Construction of Long-term Seismic Catalog with Deep Learning and Characterization of Preseismic Fault Behavior in the Ridgecrest-Coso Region (2008-2019)

Yijian Zhou[1*], Abhijit Ghosh[1], Lihua Fang[2], Han Yue[3], Shiyong Zhou[3]

[1]Department of Earth and Planetary Sciences, University of California, Riverside, USA

[2]Institute of Geophysics, China Earthquake Administration, Beijing, China

[3]Institute of Theoretical and Applied Geophysics, Peking University, Beijing, China

Corresponding author: Yijian Zhou (yijian.zhou@email.ucr.edu)

Key Points:

- The Train-Detect-Pick (TDP) strategy realizes stable and efficient phase picking performance based on deep learning.
- The Ridgecrest region has low but distributed seismicity before the earthquake, and its depth distribution delineates a persistent asperity.
- The Coso geothermal field has a high b-value that does not correlate with the seismicity rate and production data, indicating a low stress level.

Abstract

Long-term seismicity is an effective tool to infer fault properties at depth, but the catalog construction is challenging because of the large data volume. We propose a new deep learning-based workflow that follows a "Train-Detect-Pick" procedure, which solves the generalization problem in AI pickers. We apply the new workflow on the preseismic phase (2008-2019) of Ridgecrest-Coso region. Results show that the new workflow realizes efficient and stable detection, and well substitutes matched filter. Our new catalog helps characterize the preseismic fault behavior: (1) the Ridgecrest area has a distributed deformation, and the 2019-ruptured segment has a persistent asperity; (2) the central Garlock fault is unfavorable for rupture propagation, because of its discontinuous geometry and low coupling ratio; (3) the Coso geothermal field generates intense and shallow seismicity, which has a high b-value that does not correlate with seismicity rate and industrial production, thus suggest a low stress level.

Plain Language Summary

The numerous small earthquakes contain useful information on the fault properties, but to build a high-quality catalog in a decadal scale is challenging. We propose a new workflow that train neural networks with local seismic data, so that it can be applied to most cases. In the Ridgecrest-Coso region, our new workflow outperforms matched filter method in terms of the efficiency and stability. Based on the new catalog, we obtained new insights on three major fault systems in this area: (1) the Ridgecrest faults can be discernable before the mainshock in 2019, and was strongly locked; (2) the central Garlock fault is not easy to rupture, because of the complex geometry and low coupling; (3) the Coso geothermal field has intense microseismicity, which is controlled by tectonic process and its temporal behavior suggest a low stress level.

1 Introduction

Microseismicity provides a direct indication to the fault structure and slip behavior at depth. Such strategy is especially useful when the fault slips at a high rate, e.g. during early aftershocks period (e.g. Tan et al., 2021; Zhou et al., 2022a), or for creeping faults (e.g. Waldhauser and Ellsworth, 2002; Chen et al., 2020). However, a huge portion of faults generate low seismicity rate during the interseismic period because of a high locking ratio (e.g. Bletery et al., 2020; Chamberlain et al., 2021; Uchida and Bürgmann, 2021; Zhou et al., 2022b), and these faults are

also prone to large earthquakes (Sykes, 2021; Lay and Nishenko, 2022). To study the strongly locked faults, a long-term observation is always necessary. For example, Schurr et al. (2020) built a seismic catalog for 7 years before the 2014 Iquique earthquake, and found that the pre-earthquake seismicity complements the coseismic slip; Sugan et al. (2023) observed a 8-year migration of seismicity towards the nucleation area of the 2016 central Italy seismic sequence. Technically, the construction of long-term catalogs requires a workflow that is both computationally efficient and of high detection completeness, which is still a challenging task.

Currently, two types of cataloging workflow can realize a state-of-the-art performance: (1) the PAL-style workflow that follows "phase Picking – phase Association – event Location" procedure (e.g. Zhou et al., 2021b; Zhang et al., 2022; Zhu et al., 2022b), and (2) the matched filter technique (MFT) that utilizes pre-detected events as templates to detect similar events (e.g. Ross et al., 2019a; Shelly, 2020; Neves et al., 2022). The detection completeness of PAL-style workflows is basically dependent on the phase picking algorithm. In recent years, algorithms based on artificial intelligence (AI), specifically deep learning, realize outstanding phase picking performance in terms of the detectability and picking precision (e.g. Zhu and Beroza, 2018; Zhou et al., 2019; Mousavi et al., 2020). However, systematic tests show that the AI pickers can suffer from inconsistent performance among data in different regions (e.g. Chai et al., 2020; Jiang et al., 2021; Zhu et al., 2022a), which show a lower generalizability compared with traditional rule-based algorithms, such as short-term-average over long-term average (STA/LTA). The MFT methods realize even higher detection ability than AI (e.g. Mousavi et al., 2019; Zhou et al., 2021a), but its low computational efficiency makes it difficult to process big data, and the detection results may be biased by incomplete templates. In short, the AI-based picker is the most promising method that combines both high efficiency and high detectability, while further improvements are needed to realize a consistent picking performance on a large spatiotemporal range of data.

In this paper, we present a new AI-based cataloging workflow based on a "Train-Detect-Pick" (TDP) strategy, which solves the generalization problem in deep learning models. The TDP workflow is applied to the preseismic period of the Ridgecrest-Coso region during 2008-2019 to characterize its fault behavior before the 2019 M_w 7.1 Ridgecrest earthquake.

2 Cataloging Workflow based on AI Phase Picker

2.1 Train, Detect, and Pick

The AI phase pickers require large number of training samples to tune the hyper-parameters with the neural network. As reviewed in the Introduction section, the first generation of AI pickers attempt to build a pre-trained model that is suitable for all data, which is not very successful so far. Instead, we designed a new workflow that generates local training samples to train an AI model, so that it is suitable for local data (Figure 1).

In the first stage, we utilize the PAL method (Zhou et al., 2021b) to construct the training set (Figure 1). The detection process of PAL is based on STA/LTA, and can provide reliable identification of signals with high signal-noise ratio (SNR). We slice training samples with the PAL-picked P & S arrivals (see supplementary Text S1 for more details). The AI model we adopted is a hybrid method that utilizes Convolutional neural network (CNN) for Event detection and Recurrent neural network (RNN) for Phase picking (i.e. CERP, Zhou et al., 2019). It is applied to continuous data in a sliding window manner, where the sliding windows are firstly classified as earthquakes or noise by CNN (i.e. event detection), and the earthquake windows are then sent to RNN for phase picking purpose (see more details on the CERP parameters in Text S2). Note that the CERP model is more light-weighted compared to the U-net and transformer model, thus requires less training samples, as shown in the blind test by Mousavi et al. (2020).

In the second stage, we substitute the PAL picker with the locally-trained CERP picker (Figure 1). The CERP picker provide accurate detection for much weaker signals, and will approximately double the number of initial PAL event detections (e.g. Zhou et al., 2021a). We also built interface for HypoInverse (Klein, 2002) and HypoDD (Waldhauser, 2001) to relocate the CERP detections (Figure 1), among which the *ph2dt_cc* modulus calculates the high-resolution differential travel times with cross correlation (CC; details can be found in Text S3). This makes a seamless cataloging workflow that applies to continuous data.

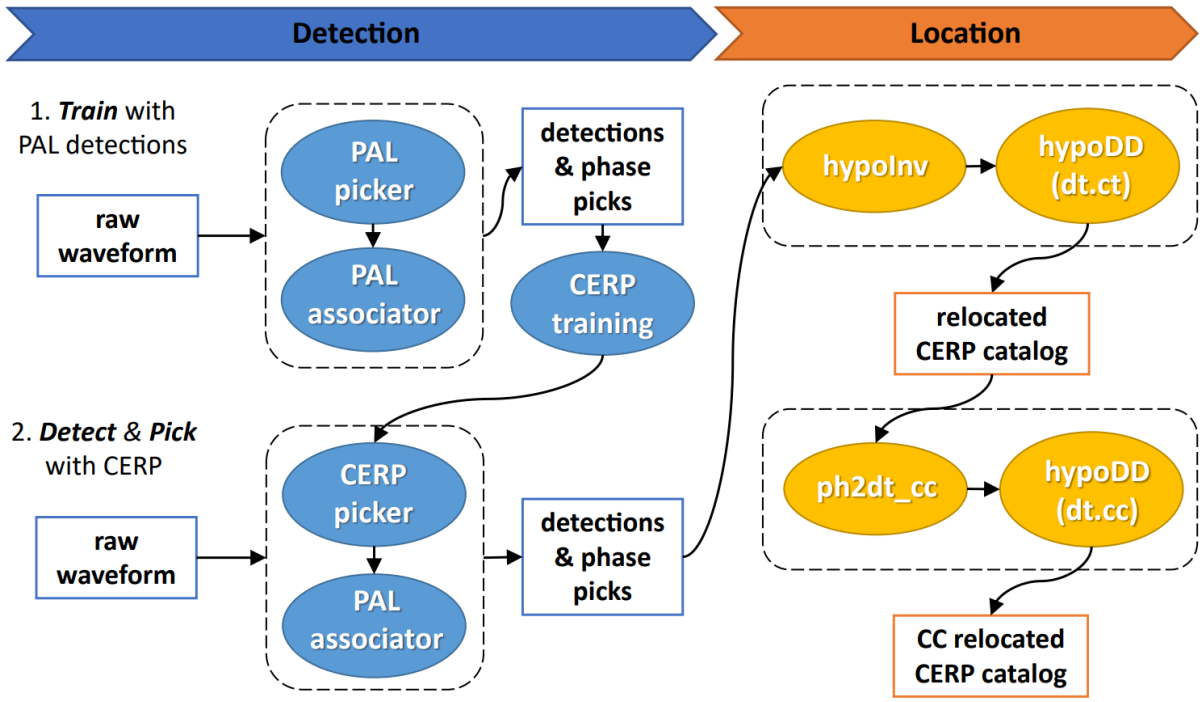

Figure 1. The TDP-style workflow for earthquake cataloging. The blue and yellow modules denote the detection and location algorithms, respectively. PAL refers to an STA/LTA-based cataloging method developed by Zhou et al. (2021b); CERP refers to a hybrid deep learning picker combining CNN Event detection and RNN Phase picking (Zhou et al., 2019).

2.2 Performance on Co- and Pre-seismic Data

We first test the new AI-based workflow on the early aftershocks of the 2019 Ridgecrest earthquake from 2019/07/04 to 2019/07/24. With the same set of permanent and temporal stations as that used by the Southern California Seismic Network (SCSN, Figure S1), adopting the same set of parameters in Zhou et al. (2021b), PAL detected 45,083 events within the source region (that in Figure 2) and 408,199 P & S pairs associated with them. For CERP, we set the window length as 12 s and sliding step as 4 s, so that the P & S waves on stations within a ~60-km epicentral distance can be covered. After applying CERP, the detection number increase to 81,142, and the relocation process finally maintains 55,662 well-located events. We compare the final CERP-TDP catalog with two other CC-relocated catalogs (Figure 2): the relocated SCSN catalog (Hauksson et al., 2012) and the QTM catalog built by MFT (Ross et al., 2019b). It is clear that the three catalogs show highly consistent map-view distribution and comparable relocation precision, despite using different relocation algorithms, parameters, and velocity models. However, the depth

distribution is less consistent, as shown in the along-strike profiles: the QTM catalog is systematically shallower by ~2 km (Figure 2b), and our CERP-TDP catalog deepens along with the coseismic slip, especially at the distance of 15-30 km (Figure 2c).

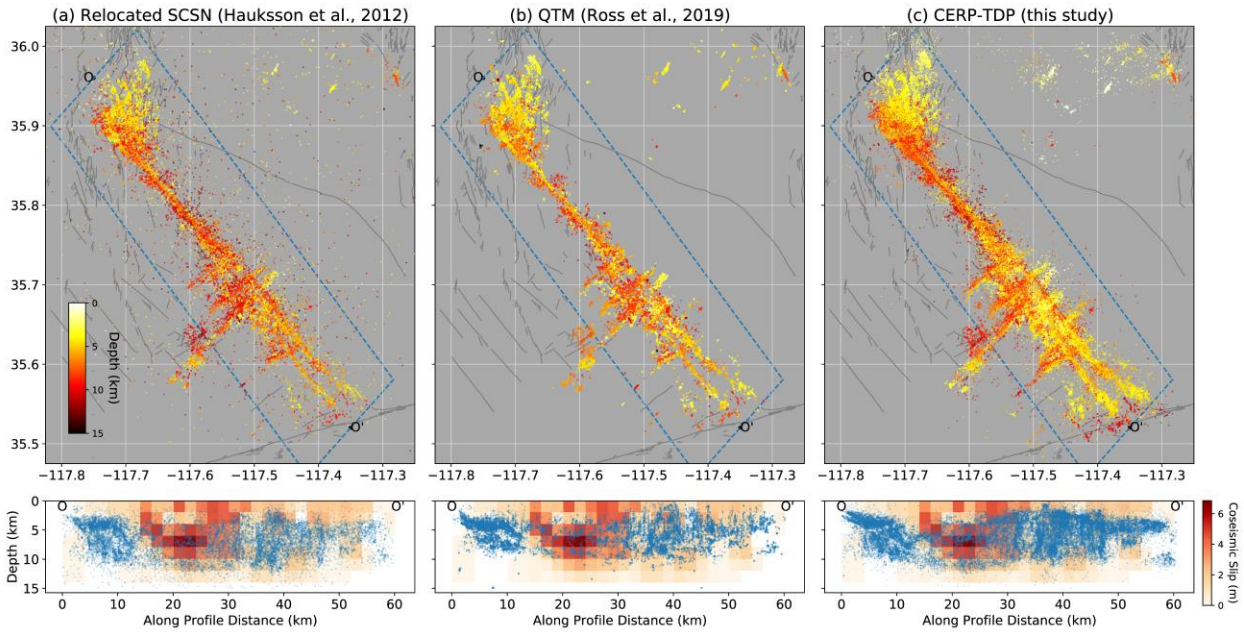

Figure 2. Comparison of aftershock relocation results. (a-c) plot the relocation results of the SCSN catalog (Hauksson et al., 2012), QTM catalog (Ross et al., 2019b), and the relocated CERP-TDP catalog in this study, respectively. The events within the blue rectangle are plotted in the profile. The coseismic slip model comes from Yue et al. (2021).

We also compare the frequency-magnitude distributions (FMD, Figure 3a-b). Results show that the QTM and CERP-TDP both realize ~3-4 times more detections than the SCSN catalog, while the QTM catalog only have ~35% of the detections well located, according to the criteria of Growclust algorithm (Trugman and Shearer, 2017). The detection completeness of the SCSN & QTM catalog seems to be inconsistent for M 0-2 and M>2 events, as shown in the FMDs that deviate from the empirical scaling law (Gutenberg and Richter, 1944). Another noteworthy feature is the change in FMD slope of the SCSN & QTM catalog at M ~3.5 (Figure 3a-b), which is partly caused by the different magnitude scales adopted (e.g. M_l ,M_w, or M_{lr}, https://scedc.caltech.edu/eq-catalogs/change-history.html), and can affect the catalog-based b-value studies.

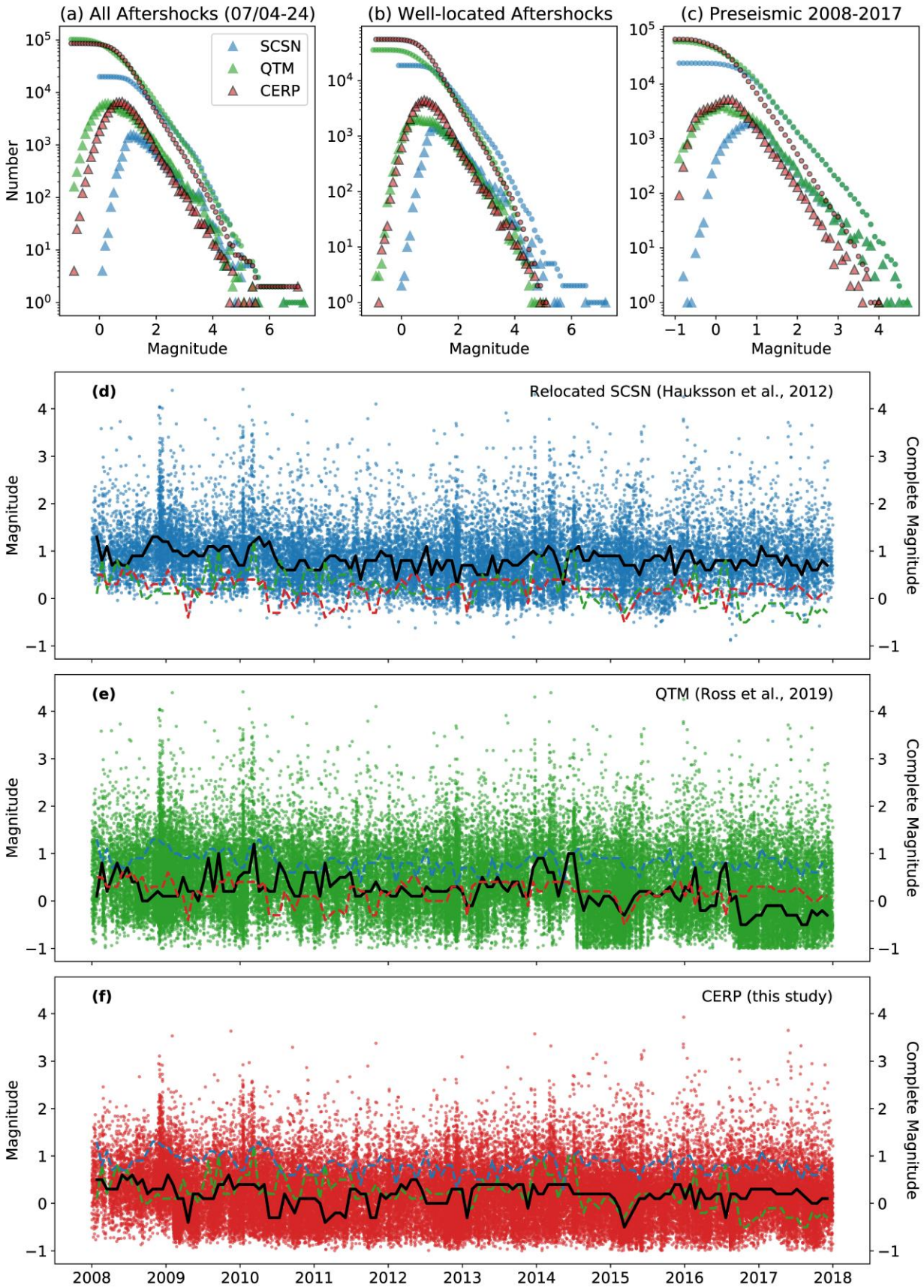
(a) All Aftershocks (07/04-24)
(b) Well-located Aftershocks
(c) Preseismic 2008-2017
SCSN
QTM
CERP
Number
Magnitude
(d)
Relocated SCSN (Hauksson et al., 2012)
(e)
QTM (Ross et al., 2019)
(f)
CERP (this study)
Magnitude
Complete Magnitude
2008
2009
2010
2011
2012
2013
2014
2015
2016
2017
2018

Figure 3. Comparison of frequency-magnitude distribution (FMD) and magnitude-time sequence. (a-c) plot the FMD comparison for the total aftershock detection, well located aftershocks, and the preseismic period starting from 2008, respectively. The dots and triangles denote cumulative and non-cumulative distribution. (d-f) plot the magnitude-time comparisons for the preseismic period. The thick black lines denote the magnitude of completeness, and the colored dash lines plot that for two other catalogs.

For the preseismic period (2008/01/01-2019/07/03), the catalog building is more difficult for several reasons: (1) only permanent stations are available (Figure S1), which is sparser around the Ridgecrest faults and is not spatially uniform; (2) nearly half of the stations experienced a change from 1-channel to 3-channel instrument around 2014 (Figure S4); (3) data glitches (i.e. instrumental noises in pulse-shape, Figure S6) takes an non-negligible amount of time. We made special treatments regarding this complex data condition, including the training of CERP picker and the weighting scheme in relocation (see Text S1 & S4 for more details). In the PAL process, we detected 70,017 earthquakes in total, along with 489,382 P & S pairs that has a S-P time <8 s, P wave SNR >12, and a P wave travel time residual <1 s. We train the CERP model under a window length of 15 s, and apply it with a sliding window step of 5 s. After the same phase association process, we finally get a total of 125,790 detections, among which 90,892 events are within the study region (inside map area in Figure 4) and 78,117 of those are well relocated. The average relative location uncertainty is ~60 m laterally and ~80 m vertically, under the least-square criteria of hypoDD (see Text S4). Note that the whole process is completed in 5 days with 1 Nvidia GeForce RTX 2080 GPU card and 1 Intel Xeon E5-2695 CPU.

Similar to the early aftershocks, we compare the CERP-TDP catalog with the relocated SCSN catalog and QTM (Figure 3c-f). Again, both CERP-TDP and QTM realize a ~1.5-fold increase of detection number compared with the SCSN catalog, and we still find a better linearity of the CERP-TDP result in the FMDs (Figure 3c), which is probably related to the change of magnitude scale through time and for different sizes of earthquakes in the SCSN catalog. In the magnitude-time comparison (Figure 3d-f), we can see that the SCSN catalog is not temporally consistent, with high detectability only during the intense seismic sequence. This temporal inconsistency is not fully solved in the QTM catalog (Figure 3e). This is probably because the seismic events in the background period and during intense sequences are generated on different faults or asperities, and their waveforms are not very similar, thus lowering down the performance of matched filter. However, our CERP-TDP catalog realize a much more stable detection through

this 10-year period (Figure 3f), which indicates that the statistical features of seismic events over a large spatiotemporal range are well captured by the neural networks.

As a summary, these comparisons show that our new TDP strategy realizes comparable earthquake detection completeness as that of the matched filter, but is more computationally efficient, more temporally stable, and gives more linear FMD. Thus, this new AI-based workflow provides a launching pad for the long-term seismicity studies.

3 Characterizing Preseismic Fault Behavior

Using our new CERP-TDP catalog, we aim to characterize the preseismic fault behavior of the Ridgecrest-Coso region by analyzing the spatiotemporal distribution of seismicity and b-value (Figure 4). This analysis is based on the idea that: (1) small earthquakes occur on faults, and its occurrence rate is proportional to the fault creep rate (e.g. Liu et al., 2022), as deduced from the simple asperity model for small earthquakes (Bürgmann, 2018; Uchida and Bürgmann, 2019); (2) the b-value, which describes the relative number of large and small earthquakes, is negatively related to the stress level, as shown in multiple experimental and statistical studies (Scholz, 2015, and references therein). Details for the b-value calculation can be found in the supporting material Text S5. Three specific fault systems are of interest (Figure 5): the faults ruptured by the 2019 Ridgecrest earthquake, the central Garlock fault, and the Coso geothermal field (CGF).

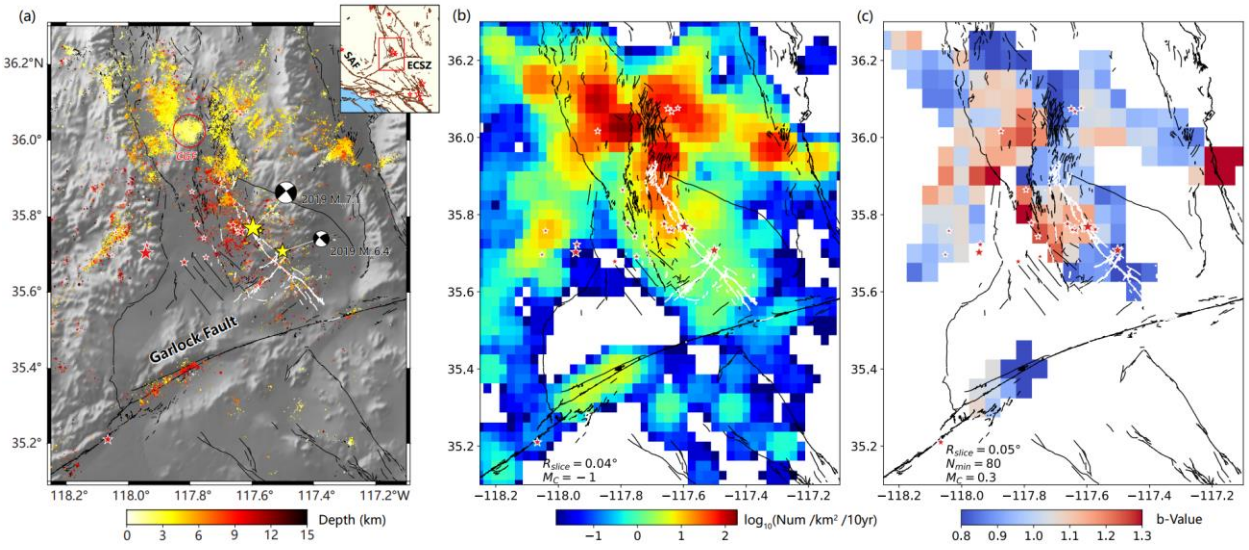

Figure 4. Seismicity and b-value analysis. (a) Seismicity distribution. Seismic events are plotted in dots coded by its focal depth. Historic events since 1946 with M >5 are plotted in red stars. The black

and white lines mark the active faults and surface rupture by the 2019 Ridgecrest earthquake, respectively. The red circle highlights the Coso geothermal field (CGF). (b) Seismicity rate. (c) b-value distribution.

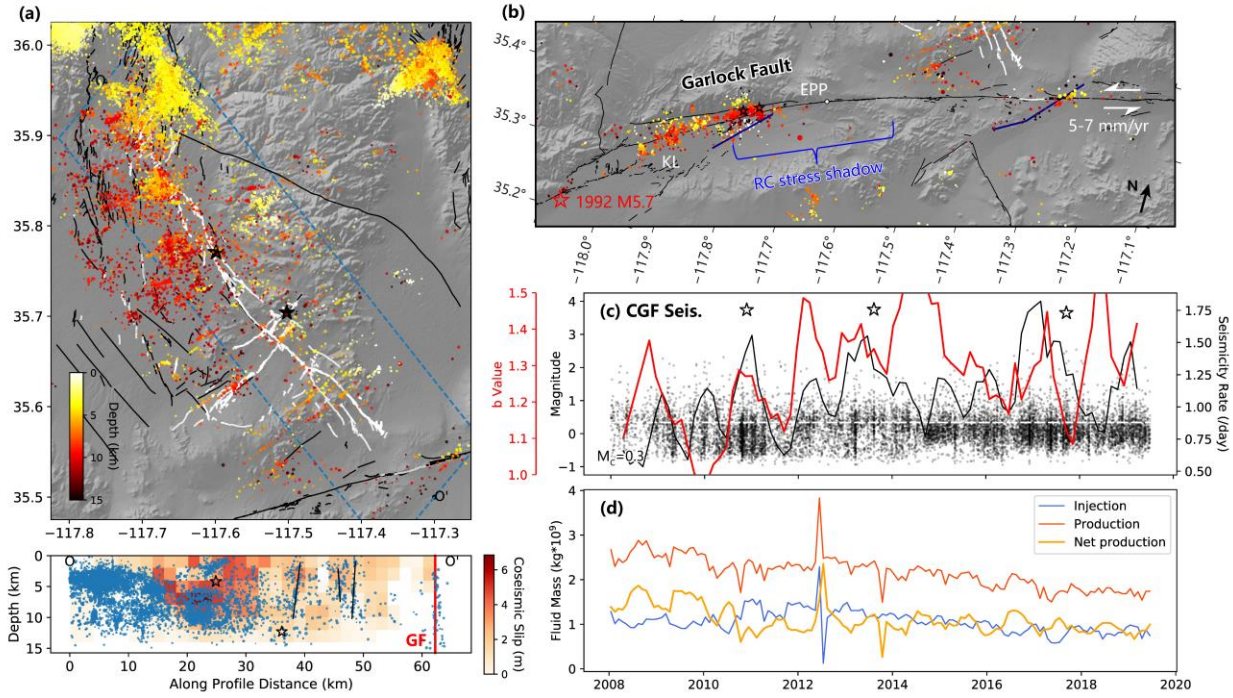

Figure 5. Spatiotemporal seismicity analysis. (a) Ridgecrest-ruptured fault. Black lines in the profile mark the interpreted conjugate structures. The vertical red line denotes the Garlock fault (GF). The 2019 foreshock and mainshock are marked by black stars. (b) Central Garlock fault. The dark-blue lines plot the unmapped conjugate faults inferred from this study. Two M>4 events are marked by black starts. The blue bracket roughly marks the stress shadow caused by the Ridgecrest earthquake. The El Paso Peaks (EPP) paleoseismic site and the Koehn Lake (KL) are also marked. (c-d) Coso geothermal field. (c) plots the comparison between the seismicity rate within CGF (the red circle in Figure 4a) and the b-value. The b-value and seismicity rate are calculated with the complete part of catalog, with the M_C set to 0.3, as marked by the white dashed line. (d) plots the geothermal production data.

3.1 2019 Ridgecrest-ruptured fault

It is well known that the 2019 Ridgecrest M_w 6.4 & 7.1 sequence ruptures a mostly unmapped orthogonal fault system (Figure 5a, Ross et al., 2019a). However, after a more detailed geological investigation, Thompson Jobe et al. (2020) found that up to 50-70% of the fault traces could have been mapped before the earthquake. It is important to know whether long-term seismicity provides more evidence on the fault existence before the earthquake.

Similar as observed in Hauksson and Jones (2020), we also find a low seismicity rate on Ridgecrest faults before the earthquake (Figure 4b). However, this ~20-km-wide band highlighted by the microseismicity is still much more active than other area with no mapped faults. It is very possible that multiple subparallel faults extent to the SE of the foreshock epicenter, where no faults are previously mapped. The net effect of such a fault system is a distributed shear deformation and a low slip rate on each fault. Moreover, by examining the depth distribution (Figure 5a), we find that the pre-earthquake seismicity is highly similar to the aftershock distribution that delineates the coseismic slip and show orthogonal faulting (Figure 2c), except for a much lower seismicity rate. This indicates that the Ridgecrest asperity is persistent through decades.

Fortunately, enough number of events are available to resolve the b-value on Ridgecrest faults (Figure 4c). We find that a low b-value is resolved surrounds the 2019 M_w 6.4 foreshock, indicating a high stress level. This is consistent with the fact that the Ridgecrest fault is strongly locked before the earthquake, and that the frictional coefficient is rather high (0.75, Hauksson and Jones, 2020). In contrast, the M_w 7.1 mainshock area is of high b-value, which can be interpreted by the stress shadow caused by several M >5 events during 1990s on its western subparallel faults. Similar preseismic b-value distribution pattern is also obtained in Nanjo (2020) with ~40-year SCSN catalog. This preseismic b-value contrast near the foreshock and mainshock epicenter can also explain the location of foreshock, and why did the M_w 6.4 come first.

Thus, (1) the distributed seismicity with a low occurrence rate near the Ridgecrest region, and (2) the overall low b-value along the Ridgecrest fault, jointly suggest a fault system consisting of multiple subparallel branches exist before the earthquake. Our results also show that the event distribution and b-value analysis can jointly delineate asperities that can generate large earthquakes.

3.2 Central Garlock fault

The central Garlock fault cuts off the Ridgecrest fault on the south, and is a major fault that accommodates the tectonic loading (McGill and Sieh, 1993; Ganev et al., 2012; Hatem and Dolan, 2018). The segmentation of Garlock fault is based on geometrical complexity, including the fault bends and stepovers, e.g. the western boundary of the central segment near the Koehn Lake stepover (KL, Figure 5b). This western end is also microseismically active for decades, and a seismic swarm is triggered after the 2019 earthquake (Ross et al., 2019a), both of which indicate a low fault coupling ratio. However, we would like to point out that the b-value for this seismic

cluster increased from west to east (Figure 4c, S11, S13), thus the eastern portion that generated 2 M~4 events during 2008-2019 (Figure 5b, S15) is probably characterized by higher fault strength. Stress modeling show that the Ridgecrest earthquake draws a Coulomb stress shadow in the middle of central Garlock fault (Nanjo, 2020; Toda and Stein, 2020). This should also be the case during the interseismic period: the slip of Ridgecrest fault unclamps the central Garlock fault, and will lower down its stress level in the long term.

To understand how such fault properties affect the dynamic rupture process, we compare the paleo-earthquake behaviors: the El Paso Peaks (EPP) paleoseismic site (Figure 5b) is roughly the termination for at least 4 consecutive earthquakes in the past ~5600 years, except for the most recent event in 1450 that went through at least the western and central segment (Dawson et al., 2003; Madden Madugo et al., 2012). This implies that the central Garlock fault may be difficult for the dynamic rupture to propagate, which is probably a joint effect of geometric complexity, low fault coupling, and low stress level. However, it is worth noting that the quiescent segment between EPP and the junction between Ridgecrest fault (Figure 5b) is probably frictionally locked at depth, considering the 1450 went-through rupture and the low seismicity rate, despite the fact that a triggered shallow creep is observed (Barnhart et al., 2019; Ross et al., 2019a).

3.3 Coso geothermal field

The Coso geothermal field (CGF) is one of the largest three geothermal fields in California, and induced seismicity has been prevalent in this region (Schoenball et al., 2015; Trugman et al., 2016, and references therein). Lying in the center of an extensional stepover, the CGF is also a tectonically active region that produces sustained and active microseismicity (Hauksson and Unruh, 2007; Hauksson and Jones, 2020). Thus, both anthropogenic and tectonic processes can affect the occurrence of microseismicity, and the relationship between these processes is of scientific interest.

As also shown in previous studies (Nanjo, 2020; Im et al., 2021), microseismicity in CFG is intense and shallow (<4 km, Figure 4a), accompanied by a high b-value (Figure 4c). This can be explained by a shallow brittle-ductile transition caused by geothermal activities, as shown in the P & S wave velocity structure (Hauksson and Unruh, 2007; Zhang and Lin, 2014), and that decades of geothermal production depleted the shear stress in CGF (Im et al., 2021). The surrounding area of CGF also generate active microseismicity, but at larger depths (Figure 4a). Interestingly, the b-value is quite different on the west and east of CGF (Figure 4c, S13), which

may be the result of different fault orientations or is related to heat flow, and further investigations are needed.

Furthermore, we examine the temporal correlation between the seismicity rate, b-value, and the geothermal production (Figure 5c-d). Results show that the seismicity rate and b-value are highly variable during 2008-2019, and they have no correlation with the production data. This negative result is consistent with previous statistics in CGF using the SCSN catalog, where the correlation between seismicity rate and production volume only exists in the initial stage of geothermal production (i.e. before 1990, Trugman et al., 2016). It indicates that the dominant factor controlling microseismic activity in CGF is not geothermal production, but tectonic processes, such as fault creep and earthquake-induced stress transfer. For example, Trugman et al. (2016) find that the b-value in CGF decrease significantly following a prominent seismic swarm on the west of CGF in 2001, which causes an steep increase in seismicity rate and decrease in b-value. Moreover, we only find a weak correlation between the seismicity rate and b-value during 2008-2019, which may imply that the CGF is less sensitive to stress triggering than around 2000. Such behavior is consistent with the fact that aftershocks are not triggered in CGF by the Ridgecrest earthquake (Im et al., 2021), remote dynamic triggering is less prominent in CGF than the surrounding area (Zhang et al., 2017), and that most area of CGF is not modulated by tidal stress (Wang et al., 2022).

4 Conclusions

In this paper, we present a new workflow to build long-term catalog using deep learning, which is based on the idea of training model on local data to avoid the generalizability problem. By applying it on the preseismic period (2008-2019) of Ridgecrest-Coso region, we find that this TDP workflow realize comparable detectability as the matched filter, but is much more computationally efficient and temporally stable. We characterize the preseismic fault behavior with our new AI catalog. Our main conclusions are:

(1) The Ridgecrest area has the shear deformation distributed over a band of ~20-km wide that comprises multiple subparallel faults. This generates a diffused and infrequent seismicity. The 2019-ruptured asperity is persistent, since the pre-earthquake seismicity distributes in the same pattern as the aftershocks, complementing the coseismic slip.

(2) The western end of central Garlock fault is a rupture barrier, because of the geometric complexity and low fault coupling. The middle segment of central Garlock fault is probably of low stress level but is frictionally locked.

(3) The seismicity in Coso geothermal field during 2008-2019 is mainly controlled by tectonic processes, since the seismicity rate and b-value does not correlate with geothermal production. The seismicity rate is not strongly correlated with the b-value as well, implying that CGF is not sensitive to stress triggering.

Acknowledgments

We thank Prof. Zhongwen Zhan, Prof. Zhigang Peng, Prof. Wenyuan Fan, Prof. Junle Jiang, and Dr. Alba Rodríguez Padilla for constructive discussions. This work is jointly supported by the US National Science Foundation (award number 1941719), Southern California Earthquake Center, University of California Riverside, the National Key R&D Program of China (grant number 2021YFC3000702), and the National Natural Science Foundation of China (grant number U2039204).

Open Research

Figures in this paper are plotted with GMT and Matplotlib. The continuous seismic data, the waveform-relocated catalog, and the QTM catalog are downloaded from SCSN (https://dx.doi.org/10.7909/C3WD3xH1). The active faults data comes from USGS https://www.usgs.gov/programs/earthquake-hazards/faults. The surface rupture data of the 2019 Ridgecrest earthquake comes from Ponti et al. (2020). The coseismic slip model comes from Yue et al. (2021). The CERP picker and related hypo-locator interfaces can be found at Github: https://github.com/YijianZhou/CERP_TDP (https://doi.org/10.5281/zenodo.6799488) and https://github.com/YijianZhou/Hypo-Interface-Py (https://doi.org/10.5281/zenodo.6968950).

References

Barnhart, W. D., G. P. Hayes, and R. D. Gold (2019). The July 2019 Ridgecrest, California, Earthquake Sequence: Kinematics of Slip and Stressing in Cross-Fault Ruptures, *Geophysical Research Letters*, *46*(21), 11859-11867, doi:https://doi.org/10.1029/2019GL084741.

Bletery, Q., O. Cavalié, J.-M. Nocquet, and T. Ragon (2020). Distribution of Interseismic Coupling Along the North and East Anatolian Faults Inferred From InSAR and GPS Data, *Geophysical Research Letters*, *47*(16), e2020GL087775, doi:https://doi.org/10.1029/2020GL087775.

Bürgmann, R. (2018). The geophysics, geology and mechanics of slow fault slip, *Earth and Planetary Science Letters*, *495*, 112-134, doi:https://doi.org/10.1016/j.epsl.2018.04.062.

Chai, C., M. Maceira, H. J. Santos-Villalobos, S. V. Venkatakrishnan, M. Schoenball, W. Zhu, G. C. Beroza, C. Thurber, and E. C. Team (2020). Using a Deep Neural Network and Transfer Learning to Bridge Scales for Seismic Phase Picking, *Geophysical Research Letters*, *47*(16), e2020GL088651, doi:https://doi.org/10.1029/2020GL088651.

Chamberlain, C. J., W. B. Frank, F. Lanza, J. Townend, and E. Warren-Smith (2021). Illuminating the Pre-, Co-, and Post-Seismic Phases of the 2016 M7.8 Kaikōura Earthquake With 10 Years of Seismicity, *Journal of Geophysical Research: Solid Earth*, *126*(8), e2021JB022304, doi:https://doi.org/10.1029/2021JB022304.

Chen, Y., K. H. Chen, J.-C. Hu, and J.-C. Lee (2020). Probing the Variation in Aseismic Slip Behavior Around an Active Suture Zone: Observations of Repeating Earthquakes in Eastern Taiwan, *Journal of Geophysical Research: Solid Earth*, *125*(5), e2019JB018561, doi:https://doi.org/10.1029/2019JB018561.

Dawson, T. E., S. F. McGill, and T. K. Rockwell (2003). Irregular recurrence of paleoearthquakes along the central Garlock fault near El Paso Peaks, California, *Journal of Geophysical Research: Solid Earth*, *108*(B7), doi:https://doi.org/10.1029/2001JB001744.

Ganev, P. N., J. F. Dolan, S. F. McGill, and K. L. Frankel (2012). Constancy of geologic slip rate along the central Garlock fault: implications for strain accumulation and release in southern California, *Geophysical Journal International*, *190*(2), 745-760, doi:10.1111/j.1365-246X.2012.05494.x.

Gutenberg, B., and C. F. Richter (1944). Frequency of earthquakes in California, *Bulletin of the Seismological Society of America*, *34*(4), 185-188, doi:10.1785/bssa0340040185.

Hatem, A. E., and J. F. Dolan (2018). A Model for the Initiation, Evolution, and Controls on Seismic Behavior of the Garlock Fault, California, *Geochemistry, Geophysics, Geosystems*, *19*(7), 2166-2178, doi:https://doi.org/10.1029/2017GC007349.

Hauksson, E., and J. Unruh (2007). Regional tectonics of the Coso geothermal area along the intracontinental plate boundary in central eastern California: Three-dimensional Vp and Vp/Vs models, spatial-temporal seismicity patterns, and seismogenic deformation, *Journal of Geophysical Research: Solid Earth*, *112*(B6), doi:https://doi.org/10.1029/2006JB004721.

Hauksson, E., W. Yang, and P. M. Shearer (2012). Waveform Relocated Earthquake Catalog for Southern California (1981 to June 2011), *Bulletin of the Seismological Society of America*, *102*(5), 2239-2244, doi:10.1785/0120120010.

Hauksson, E., and L. M. Jones (2020). Seismicity, Stress State, and Style of Faulting of the Ridgecrest - Coso Region from the 1930s to 2019: Seismotectonics of an Evolving Plate

Boundary Segment, *Bulletin of the Seismological Society of America*, *110*(4), 1457-1473, doi:10.1785/0120200051.

Im, K., J.-P. Avouac, E. R. Heimisson, and D. Elsworth (2021). Ridgecrest aftershocks at Coso suppressed by thermal destressing, *Nature*, *595*(7865), 70-74, doi:10.1038/s41586-021-03601-4.

Jiang, C., L. Fang, L. Fan, and B. Li (2021). Comparison of the earthquake detection abilities of PhaseNet and EQTransformer with the Yangbi and Maduo earthquakes, *Earthquake Science*, *34*(5), 425-435, doi:10.29382/eqs-2021-0038.

Klein, F. W. (2002). User's guide to HYPOINVERSE-2000, a Fortran program to solve for earthquake locations and magnitudes*Rep. 2331-1258*, US Geological Survey.

Lay, T., and S. P. Nishenko (2022). Updated concepts of seismic gaps and asperities to assess great earthquake hazard along South America, *Proceedings of the National Academy of Sciences*, *119*(51), e2216843119, doi:doi:10.1073/pnas.2216843119.

Liu, Y.-K., Z. E. Ross, E. S. Cochran, and N. Lapusta (2022). A unified perspective of seismicity and fault coupling along the San Andreas Fault, *Science Advances*, *8*(8), eabk1167, doi:doi:10.1126/sciadv.abk1167.

Madden Madugo, C., J. F. Dolan, and R. D. Hartleb (2012). New Paleoearthquake Ages from the Western Garlock Fault: Implications for Regional Earthquake Occurrence in Southern California, *Bulletin of the Seismological Society of America*, *102*(6), 2282-2299, doi:10.1785/0120110310.

McGill, S., and K. Sieh (1993). Holocene slip rate of the Central Garlock Fault in southeastern Searles Valley, California, *Journal of Geophysical Research: Solid Earth*, *98*(B8), 14217-14231, doi:https://doi.org/10.1029/93JB00442.

Mousavi, S. M., W. Zhu, Y. Sheng, and G. C. Beroza (2019). CRED: A Deep Residual Network of Convolutional and Recurrent Units for Earthquake Signal Detection, *Scientific Reports*, *9*(1), 10267, doi:10.1038/s41598-019-45748-1.

Mousavi, S. M., W. L. Ellsworth, W. Zhu, L. Y. Chuang, and G. C. Beroza (2020). Earthquake transformer—an attentive deep-learning model for simultaneous earthquake detection and phase picking, *Nature Communications*, *11*(1), 3952, doi:10.1038/s41467-020-17591-w.

Nanjo, K. Z. (2020). Were changes in stress state responsible for the 2019 Ridgecrest, California, earthquakes?, *Nature Communications*, *11*(1), 3082, doi:10.1038/s41467-020-16867-5.

Neves, M., Z. Peng, and G. Lin (2022). A High‐Resolution Earthquake Catalog for the 2004 Mw 6 Parkfield Earthquake Sequence Using a Matched Filter Technique, *Seismological Research Letters*, *94*(1), 507-521, doi:10.1785/0220220206.

Ponti, D. J., et al. (2020). Documentation of Surface Fault Rupture and Ground‐Deformation Features Produced by the 4 and 5 July 2019 Mw 6.4 and Mw 7.1 Ridgecrest Earthquake Sequence, *Seismological Research Letters*, *91*(5), 2942-2959, doi:10.1785/0220190322.

Ross, Z. E., et al. (2019a). Hierarchical interlocked orthogonal faulting in the 2019 Ridgecrest earthquake sequence, *Science*, *366*(6463), 346-351, doi:10.1126/science.aaz0109.

Ross, Z. E., D. T. Trugman, E. Hauksson, and P. M. Shearer (2019b). Searching for hidden earthquakes in Southern California, *Science*, *364*(6442), 767-771, doi:10.1126/science.aaw6888.

Schoenball, M., N. C. Davatzes, and J. M. G. Glen (2015). Differentiating induced and natural seismicity using space-time-magnitude statistics applied to the Coso Geothermal field, *Geophysical Research Letters*, *42*(15), 6221-6228, doi:https://doi.org/10.1002/2015GL064772.

Scholz, C. H. (2015). On the stress dependence of the earthquake b value, *Geophysical Research Letters*, *42*(5), 1399-1402, doi:10.1002/2014gl062863.

Schurr, B., M. Moreno, A. M. Tréhu, J. Bedford, J. Kummerow, S. Li, and O. Oncken (2020). Forming a Mogi Doughnut in the Years Prior to and Immediately Before the 2014 M8.1 Iquique, Northern Chile, Earthquake, *Geophysical Research Letters*, *47*(16), e2020GL088351, doi:https://doi.org/10.1029/2020GL088351.

Shelly, D. R. (2020). A High‐Resolution Seismic Catalog for the Initial 2019 Ridgecrest Earthquake Sequence: Foreshocks, Aftershocks, and Faulting Complexity, *Seismological Research Letters*, *91*(4), 1971-1978, doi:10.1785/0220190309.

Sugan, M., S. Campanella, L. Chiaraluce, M. Michele, and A. Vuan (2023). The unlocking process leading to the 2016 Central Italy seismic sequence, *Geophysical Research Letters*, *n/a*(n/a), e2022GL101838, doi:https://doi.org/10.1029/2022GL101838.

Sykes, L. R. (2021). Decadal seismicity prior to great earthquakes at subduction zones: Roles of major asperities and low-coupling zones, *International Journal of Geosciences*, *12*(9), 845-926, doi:https://doi.org/10.4236/ijg.2021.129046.

Tan, Y. J., F. Waldhauser, W. L. Ellsworth, M. Zhang, W. Zhu, M. Michele, L. Chiaraluce, G. C. Beroza, and M. Segou (2021). Machine‐Learning‐Based High‐Resolution Earthquake Catalog Reveals How Complex Fault Structures Were Activated during the 2016–2017 Central Italy Sequence, *The Seismic Record*, *1*(1), 11-19, doi:10.1785/0320210001.

Thompson Jobe, J. A., et al. (2020). Evidence of Previous Faulting along the 2019 Ridgecrest, California, Earthquake Ruptures, *Bulletin of the Seismological Society of America*, *110*(4), 1427-1456, doi:10.1785/0120200041.

Toda, S., and R. S. Stein (2020). Long‐ and Short‐Term Stress Interaction of the 2019 Ridgecrest Sequence and Coulomb‐Based Earthquake Forecasts, *Bulletin of the Seismological Society of America*, *110*(4), 1765-1780, doi:10.1785/0120200169.

Trugman, D. T., P. M. Shearer, A. A. Borsa, and Y. Fialko (2016). A comparison of long-term changes in seismicity at The Geysers, Salton Sea, and Coso geothermal fields, *Journal of Geophysical Research: Solid Earth*, *121*(1), 225-247, doi:https://doi.org/10.1002/2015JB012510.

Trugman, D. T., and P. M. Shearer (2017). GrowClust: A Hierarchical Clustering Algorithm for Relative Earthquake Relocation, with Application to the Spanish Springs and Sheldon, Nevada, Earthquake Sequences, *Seismological Research Letters*, *88*(2A), 379-391, doi:10.1785/0220160188.

Uchida, N., and R. Bürgmann (2019). Repeating Earthquakes, *Annual Review of Earth and Planetary Sciences*, *47*(1), 305-332, doi:10.1146/annurev-earth-053018-060119.

Uchida, N., and R. Bürgmann (2021). A Decade of Lessons Learned from the 2011 Tohoku-Oki Earthquake, *Reviews of Geophysics*, *59*(2), e2020RG000713, doi:https://doi.org/10.1029/2020RG000713.

Waldhauser, F. (2001). hypoDD--A program to compute double-difference hypocenter locations, *U.S. Geological Survey Open-File Report 01-113*, 25 pp.

Waldhauser, F., and W. L. Ellsworth (2002). Fault structure and mechanics of the Hayward Fault, California, from double-difference earthquake locations, *Journal of Geophysical Research: Solid Earth*, *107*(B3), ESE 3-1-ESE 3-15, doi:10.1029/2000jb000084.

Wang, W., P. M. Shearer, J. E. Vidale, X. Xu, D. T. Trugman, and Y. Fialko (2022). Tidal modulation of seismicity at the Coso geothermal field, *Earth and Planetary Science Letters*, *579*, 117335, doi:https://doi.org/10.1016/j.epsl.2021.117335.

Yue, H., J. Sun, M. Wang, Z. Shen, M. Li, L. Xue, W. Lu, Y. Zhou, C. Ren, and T. Lay (2021). The 2019 Ridgecrest, California earthquake sequence: Evolution of seismic and aseismic slip on an orthogonal fault system, *Earth and Planetary Science Letters*, *570*, 117066, doi:https://doi.org/10.1016/j.epsl.2021.117066.

Zhang, M., M. Liu, T. Feng, R. Wang, and W. Zhu (2022). LOC‐FLOW: An End‐to‐End Machine Learning‐Based High‐Precision Earthquake Location Workflow, *Seismological Research Letters*, *93*(5), 2426-2438, doi:10.1785/0220220019.

Zhang, Q., and G. Lin (2014). Three-dimensional Vp and Vp/Vs models in the Coso geothermal area, California: Seismic characterization of the magmatic system, *Journal of Geophysical Research: Solid Earth*, *119*(6), 4907-4922, doi:https://doi.org/10.1002/2014JB010992.

Zhang, Q., G. Lin, Z. Zhan, X. Chen, Y. Qin, and S. Wdowinski (2017). Absence of remote earthquake triggering within the Coso and Salton Sea geothermal production fields, *Geophysical Research Letters*, *44*(2), 726-733, doi:https://doi.org/10.1002/2016GL071964.

Zhou, Y., H. Yue, Q. Kong, and S. Zhou (2019). Hybrid Event Detection and Phase‐Picking Algorithm Using Convolutional and Recurrent Neural Networks, *Seismological Research Letters*, *90*(3), 1079-1087, doi:10.1785/0220180319.

Zhou, Y., A. Ghosh, L. Fang, H. Yue, S. Zhou, and Y. Su (2021a). A high-resolution seismic catalog for the 2021 MS6.4/MW6.1 Yangbi earthquake sequence, Yunnan, China: Application of AI picker and matched filter, *Earthquake Science*, *34*(5), 390-398, doi:https://doi.org/10.29382/eqs-2021-0031.

Zhou, Y., H. Yue, L. Fang, S. Zhou, L. Zhao, and A. Ghosh (2021b). An Earthquake Detection and Location Architecture for Continuous Seismograms: Phase Picking, Association, Location, and Matched Filter (PALM), *Seismological Research Letters*, *93*(1), 413-425, doi:10.1785/0220210111.

Zhou, Y., C. Ren, A. Ghosh, H. Meng, L. Fang, H. Yue, S. Zhou, and Y. Su (2022a). Seismological Characterization of the 2021 Yangbi Foreshock-Mainshock Sequence, Yunnan, China: More than a Triggered Cascade, *Journal of Geophysical Research: Solid Earth*, *127*(8), e2022JB024534, doi:https://doi.org/10.1029/2022JB024534.

Zhou, Y., H. Yue, S. Zhou, L. Fang, Y. Zhou, L. Xu, Z. Liu, T. Wang, L. Zhao, and A. Ghosh (2022b). Microseismicity along Xiaojiang Fault Zone (Southeastern Tibetan Plateau) and the characterization of interseismic fault behavior, *Tectonophysics*, *833*, 229364, doi:https://doi.org/10.1016/j.tecto.2022.229364.

Zhu, J., Z. Li, and L. Fang (2022a). USTC-Pickers: a Unified Set of seismic phase pickers Transfer learned for China, *Earthquake Science*, *36*, 1-11.

Zhu, W., and G. C. Beroza (2018). PhaseNet: a deep-neural-network-based seismic arrival-time picking method, *Geophysical Journal International*, *216*(1), 261-273, doi:10.1093/gji/ggy423.

Zhu, W., A. B. Hou, R. Yang, A. Datta, S. M. Mousavi, W. L. Ellsworth, and G. C. Beroza (2022b). QuakeFlow: a scalable machine-learning-based earthquake monitoring workflow with cloud computing, *Geophysical Journal International*, *232*(1), 684-693, doi:10.1093/gji/ggac355.